Clinical Cancer Research

Multimodal Image-Guided Surgical and Photodynamic Interventions in Head and Neck Cancer: From Primary Tumor to Metastatic Drainage

Nidal Muhanna[1,2], Liyang Cui[1,3,4], Harley Chan[1,2], Laura Burgess[1,3], Cheng S. Jin[1,5,6], Thomas D. MacDonald[1,5], Elizabeth Huynh[1,3], Fan Wang[4], Juan Chen[1], Jonathan C. Irish[1,2], and Gang Zheng[1,3,5,6]

Abstract

Purpose: The low survival rate of head and neck cancer (HNC) patients is attributable to late disease diagnosis and high recurrence rate. Current HNC staging has inadequate accuracy and low sensitivity for effective diagnosis and treatment management. The multimodal porphyrin lipoprotein-mimicking nanoparticle (PLP), intrinsically capable of positron emission tomography (PET), fluorescence imaging, and photodynamic therapy (PDT), shows great potential to enhance the accuracy of HNC staging and potentially HNC management.

Experimental Design: Using a clinically relevant VX-2 buccal carcinoma rabbit model that is able to consistently develop metastasis to regional lymph nodes after tumor induction, we investigated the abilities of PLP for HNC diagnosis and management.

Results: PLPs facilitated accurate detection of primary tumor and metastatic nodes (their PET image signal to surrounding muscle ratios were 10.0 and 7.3, respectively), and provided visualization of the lymphatic drainage from tumor to regional lymph nodes by both preoperative PET and intraoperative fluorescence imaging, allowing the identification of unknown primaries and recurrent tumors. PLP-PDT significantly enhanced cell apoptosis in mouse tumors (73.2% of PLP-PDT group vs 7.1% of PLP alone group) and demonstrated complete eradication of primary tumors and obstruction of tumor metastasis in HNC rabbit model without toxicity in normal tissues or damage to adjacent critical structures.

Conclusions: PLPs provide a multimodal imaging and therapy platform that could enhance HNC diagnosis by integrating PET/computed tomography and fluorescence imaging, and improve HNC therapeutic efficacy and specificity by tailoring treatment via fluorescence-guided surgery and PDT. *Clin Cancer Res; 22(4); 961–70. ©2015 AACR.*

Introduction

Head and neck cancer (HNC) annually accounts for more than 550,000 new cancer cases (1) and approximately 350,000 cancer deaths, worldwide (2). HNCs are a heterogeneous group of tumors that arise in the head and neck area and are notorious for their high morbidity, aggressive behavior, and requirement for multidisciplinary care. HNCs have large variations in etiologies, anatomical, prognoses, and tumor stages (3–6). HNC patients with oral cavity cancer exhibit an average 50% to 55% 5-year survival rate. Prognosis is dependent on the stage of the tumor at the initial presentation and its accuracy is critical for appropriate treatment management (7, 8). The proximity of HNC to several adjacent critical structures, such as major vessels, cranial nerves, sensory organs, and the brain, also increases the importance of accurate assessment of local and regional disease to optimize effective tumor removal and disease-specific treatment.

Surgical resection and radiotherapy, often combined with chemotherapy, are the mainstays of HNC treatment and have increased the need for imaging modalities to guide precise treatment as any tumor that remains undetected outside of the treatment field could adversely affect the patients' prognosis and survival. The most common imaging modalities in HNC are computed tomography (CT), magnetic resonance imaging (MRI; ref. 9), single photon emission computed tomography (SPECT; ref. 10), and PET using ^{18}F-fluorodeoxyglcuose (^{18}F-FDG; refs. 11–13). However, they are often limited by inadequate sensitivity, specificity and spatial resolution for detection of small, early stage lesions and distant metastases. In addition, successfully utilizing these modalities to directly guide treatment remains a challenge. For example, determining the tumor-free margin during surgery is

[1]Princess Margaret Cancer Centre and Techna Institute, University Health Network, Toronto, Canada. [2]Department of Otolaryngology-Head and Neck Surgery, University of Toronto, Toronto, Canada. [3]Department of Medical Biophysics, University of Toronto, Toronto, Canada. [4]Medical Isotopes Research Center, Peking University, Beijing, China. [5]Department of Pharmaceutical Sciences, University of Toronto, Toronto, Canada. [6]Institute of Biomaterials and Biomedical Engineering, University of Toronto, Toronto, Canada.

Note: Supplementary data for this article are available at Clinical Cancer Research Online (http://clincancerres.aacrjournals.org/).

N. Muhanna and L. Cui contributed equally to this article.

Corresponding Authors: Gang Zheng, University Health Network, 101 College Street, TMDT 5-354, Toronto, ON M5G 1L7, Canada. Phone: 416-581-7666; Fax: 416-581-7667; E-mail: gang.zheng@uhnres.utoronto.ca; Jonathan C. Irish, University of Toronto, 190 Elizabeth Street, Toronto, Ontario, M5G 2C4, Canada. E-mail: Jonathan.Irish@uhn.ca; and Juan Chen, UHN, TMDT 5-353, 101 College Street, Toronto, ON M5G 1L7, Canada. E-mail: juan.chen@uhnresearch.ca

doi: 10.1158/1078-0432.CCR-15-1235

Translational Relevance

This translational study in a clinically relevant large animal head and neck cancer (HNC) model, provides a firm basis for future applications of porphyrin lipoprotein-mimicking nanoparticles (PLPs) in HNC management: (i) noninvasive PET imaging of unknown primary and recurrence/remnant disease based on the ability of copper-64 labeling PLPs to selectively accumulate in primary tumors and metastatic nodes with sensitive detection of lymphatic drainage; (ii) real-time intraoperative fluorescence guidance to augment current surgical procedures, including a transoral approach for oral and oropharynx primary disease and transcervical approach for neck dissection and metastatic lymph node dissection; (iii) PLP-enabled photodynamic therapy intervention either for surgically inaccessible tumors or those which are adjacent to critical anatomical structures that may be sensitive to damage during surgery.

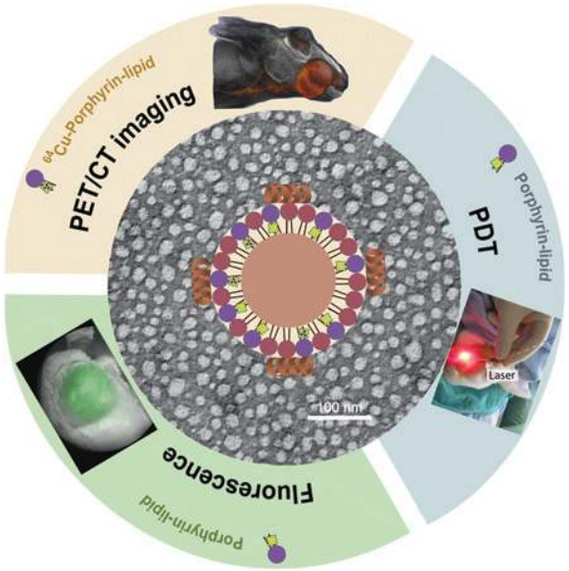

Figure 1.
Schematic presentation of PLP illustrating its core-shell spherical structure (shown in the center) with TEM image showing its size around 20 nm. Surrounding images demonstrate its intrinsic multimodalities of PET, fluorescence imaging, and PDT in a large rabbit HNC model.

still done by visual inspection and palpation. Theranostics, which integrates imaging with therapeutic functionalities into the same multimodal agent, is uniquely positioned in cancer management applications, where imaging modalities can not only noninvasively detect and functionally characterize disease, but also provide quantitative assessments of distribution and delivery of therapeutics. Theranostics thus holds great promise to traverse the gap between diagnosis and treatment to permit image-guided disease stratification and treatment (14).

In addition to the aggressive and recurrent nature of HNC, current HNC treatments involve a very high risk of functional and cosmetic debilitation to the head and neck area, which may cause collateral healthy tissue damage and long-term side effects. Therefore, a significant clinical interest is to explore alternative treatment modalities that have fewer and smaller risks but retain a high level of efficacy to improve treatment outcomes and overall quality of life. Photodynamic therapy (PDT), which generates cytotoxic singlet oxygen through interactions between optical light and a photosensitizer in the presence of oxygen, has emerged as a viable tool for localized treatment of malignant tissues (15–17). Because of the extremely short life time and subsequent short diffusion distance (10–300 nm) of singlet oxygen, PDT damage is restricted to photosensitizer accumulation, enabling local tumor ablation without damaging underlining connective tissues unlike other ablation techniques (18, 19).

Recently, we developed a novel biomimetic, porphyrin lipoprotein-mimicking nanoparticle (PLP), which integrates multiple functionalities, including PET, near-infrared (NIR) fluorescence imaging, and PDT into an ultra-small (~20 nm) nanoscaffold (20). Intrinsic copper-64 labeling allows for preoperative PET imaging of PLP delivery as well as sensitive and accurate detection of various primary and metastatic tumor types in mouse models. Its smaller size and prompt intracellular uptake compared with previously reported porphysome nanoparticles (21, 22) result in more efficient nanostructure accumulation and dissociation in tumors. This fast accumulation and dissociation releases fluorescence and photodynamic reactivity, which are highly-silenced in intact PLP, providing an attractive activation mechanism for low-background NIR fluorescence imaging and tumor-selective PDT (20).

Here, we propose novel strategies for effective HNC management using PLP-based imaging and intervention in a large animal model (orthotopic VX-2 rabbit HNC tumor model; Fig. 1): (i) PET imaging for preoperative detection of primary tumor and metastatic disease, including lymph node mapping; (ii) selective fluorescence activation in tumors to enable intraoperative visualization of tumor tissue and metastatic lymph node drainage for surgical guidance; (iii) for the first time, proof of complete ablation of primary tumors and effective prevention of tumor metastasis by image-guided PDT. Importantly, with both PLP administration and PLP induced-PDT, minimal toxicity to healthy tissues was observed. Therefore, the intrinsic multimodal and biomimetic nature of PLP confers high potential as a cancer theranostic agent for clinical translation and targeted cancer therapy.

Materials and Methods

1, 2-dimyristoyl-sn-glycero-3-phosphocholine (DMPC) was purchased from Avanti Polar Lipids Inc. Porphyrin-lipid (pyropheophorbide-lipid) was prepared using previously reported protocols (22). Cholesteryl oleate (CO) was obtained from Sigma-Aldrich Co. The ApoA-1 mimetic peptide (R4F), Ac-FAEKFKEAVKDY-FAKFWD, was purchased from GL Biochem Ltd.. Cell culture media were obtained from the ATCC (American Type Culture Collection). FBS and trypsin-ethylenediaminetetraacetic acid (EDTA) solution were all purchased from Gibco (Invitrogen Co). $^{64}CuCl_2$ was obtained from Washington University (St. Louis, MO).

PLP preparation and ^{64}Cu labeling

A lipid film was prepared by evaporation of lipid mixtures in chloroform under nitrogen. The lipid mixture for PLP consists

of 0.9 μmol porphyrin-lipid, 2.1 μmol DMPC, and 0.3 μmol cholesterol oleate. The completely dried lipid films were hydrated with 1.0 mL PBS buffer (150 mmol/L, pH 7.5) and sonicated (Bioruptor) at low frequency (30 seconds on/30 seconds off) for 30 cycles at 40°C. R4F peptide (2.3 mg, 5 mg/mL) was titrated into the rehydrated solution. After overnight shaking at 4°C, the solution was filtered with 0.1 μm membrane (Millex; Sigma-Aldrich) to gain PLP. PLP was labeled with ^{64}Cu using the previously reported method (20). Briefly, PLP was 1:1 diluted with 0.1 mol/L NH_4OAC (pH 5.5), and then mixed with $^{64}CuCl_2$ solution and incubated at 37°C for 60 minutes. The mixture was purified with the centrifugal units (30K, Amicon Ultra) and the radiochemical purity and yield were assessed.

PDT study on mouse xenograft models

All animal studies were conducted in the Animal Resource Center of the University Health Network in accordance with protocols approved by the Animal Care Committee. The PDT efficacy of PLP was investigated on KB xenograft mice. Four groups were included in the treatment study: blank control group, PDT laser alone, PLP injection alone, and PLP plus PDT laser treatment ($n = 3$ for each group). When the tumor reached 4.0 to 5.0 mm in diameter, PLP was intravenously injected into mice for the PLP group and PDT group at a dose of 5 mg/kg of porphyrin content. At 24 hours after injection, mice were anesthetized and imaged by the *in vivo* Maestro imager to evaluate tumor accumulation and porphyrin fluorescence activation. Tumors were subsequently irradiated with a 671 nm laser (DPSS LaserGlow Technologies) with a light dose of 75 J/cm^2, laser intensity of 100 mW/cm^2, and irradiation area of 9 mm diameter. Temperature changes of tumors were monitored using an infrared thermal camera (Mikroshot, LUMASENSE Technologies). Tumors from each treatment group were harvested at 24 hours after treatment, sliced, and subjected to hematoxylin and eosin (H&E) staining and TUNEL staining analysis. Cells showing DAB staining positive and with morphology of cytoplasmic condensation, loss of cell–cell contact, and shape of shrinkage were counted as TUNEL-positive cells.

VX-2 buccal carcinoma rabbit model

The VX-2 buccal squamous cell carcinoma model was developed using the method described elsewhere (23, 24). Briefly, the tumor was harvested under sterile conditions from the freshly euthanized rabbit, placed in Hank's balanced salt solution (HBSS; Sigma), washed twice with sterile HBSS, cut into small pieces, and stored at −80°C until used. To obtain a single tumor cell suspension, the tumor pieces were thawed, minced and pressed through a 70 μm cell strainer. Three hundred microliters of a high-density single-cell suspension (~5×10^6/mL) was injected into the buccinator muscle (Buccal area) of an anaesthetized New Zealand white rabbit (2.8–3.3 kg).

Pharmacokinetic study on HNC rabbits

About 2 weeks after tumor induction when the tumor size reached 1.5 to 2.0 cm, rabbits were intravenously injected with ^{64}Cu-PLP through a catheter in the marginal ear vein (0.33 mg/kg for porphyrin, ~5 mCi). Arterial blood was collected at 5 minutes, and 0.5, 1, 4, 8, 21, and 30 hours after injection ($n = 4$). The radioactivity of the plasma was determined as a function of concentration on a gamma-counter (Wizard 1480: PerkinElmer Inc.). The clearance half-life was determined by log-linear regression.

PET/CT imaging of HNC rabbits

At 24 hours after injection of ^{64}Cu-PLP (0.33 mg/kg for porphyrin, ~5 mCi), rabbits were anesthetized and subjected to PET imaging on a microPET system (Focus 220: Siemens), and CT imaging on a microCT system (Locus Ultra: GE Healthcare) following 5 mL injections of Omnipaque 350 (GE Healthcare). PET/CT Images were registered and merged using Amira (FEI Visualization Sciences Group). Volumes of interest were drawn on the merged CT images with Inveon Research Workplace (Siemens), and the standard uptake values (SUV) of ^{64}Cu-PLP were quantified from the registered images.

Biodistribution and *ex vivo* fluorescence imaging of PLP on HNC rabbits

After PET/CT imaging of rabbits, the organs (including tumors), lymph nodes, salivary glands, lungs, hearts, livers, muscles, spleen, and kidneys were excised, weighed, and their radioactivity was measured on a gamma counter. Organ uptake was calculated as percentage of injected dose per percentage of total animal mass of the sample (SUV) for each rabbit. *Ex vivo* fluorescence imaging was performed with the Maestro (Caliper Life Sciences) with a yellow filter setting (excitation: 575–605 nm; emission: ≥645 nm detection, 200 ms exposure time).

Rabbit tissue pathology and microscopic imaging

Frozen tissue sections were fixed and treated with DAPI, H&E, and Pan-Cytokeratin (PanCK) staining. High-resolution images of the stained sections were acquired on a scanning laser confocal microscope (TISSUEscope 4000, Huron Technologies).

Intraoperative fluorescence imaging

Real-time fluorescence-guided surgery on VX-2 rabbits was performed with an in-house fluorescence imaging endoscopy system (650 ± 20 nm excitation, 700 ± 25 nm emission) at 24 hours after intravenous injection of 4 mg/kg of PLP. Guided with fluorescence, tumor and suspicious lymph nodes were dissected until only nonfluorescent nodules were left on the surgical bed of the animals.

PDT on HNC rabbits

Four groups of VX-2 rabbits were included in the treatment study: blank control ($n = 3$); PDT laser alone ($n = 3$); PLP injection alone ($n = 3$); PLP plus PDT laser treatment ($n = 4$). When the tumor size reached approximately 300 mm^3, PLP was intravenously injected into rabbits for the PLP group and PLP-PDT group (4 mg/kg of porphyrin dose). For PDT treatment, rabbits were anesthetized and subjected to a two-step PDT procedure at 24 hours after injection. The first step was a straight laser irradiation (671 nm) on the exterior surface of the tumor with a light dose of 125 J/cm^2, laser power of 200 mW, and irradiation area of 15 mm in diameter. Temperature changes of tumors during laser irradiation were monitored using the infrared thermal camera. The second treatment step involved the insertion of a fiber optic cable (9 mm diffuse laser fiber) into the tumor to irradiate from the interior of the tumor with a light dose of 120 J/cm^2 and laser power of 100 mW. After the treatment, rabbits were put under a standard protocol of care and the tumor growth was continuously monitored with microCT scanning. Terminal surgeries were performed on rabbits when the tumor size reached 5,000 mm^3. All four PLP-PDT rabbits were found tumor-free at

about 30 days after treatment. They were euthanized at days 34 to 36 after PDT for further evaluation of treatment efficacy.

To evaluate the toxicity of the treatment, comprehensive biochemistry and hematology blood test of all treated rabbits were performed at 24 hours after injection, right before PDT, 1 week after, and 3 weeks after PDT treatment. After terminal surgery, tissues from tumor region and other major organs were harvested, subjected to H&E and Pan-cytokeratin staining, and imaged with Aperio ImageScope to determine the remnant of malignancy. Two experienced pathologists evaluated all histopathology slides for malignancy identification and tumor eradication confirmation.

Statistical analysis

The Student *t* test (two tailed) was used to determine significant differences in TUNEL and toxicity study. *P* values less than 0.05 were considered significant.

Results

PLP preparation and its multifunctional nature

PLP nanoparticles were prepared by assembly of porphyrin-phospholipids and DMPC-phospholipids (3:7 mol/mol) on a cholesteryl oleate core in aqueous solution, followed by size-constraint with an 18-amino acid ApoA-1 mimetic peptide R4F to obtain an ultra small spherical structure with a 20 nm average diameter (Fig. 1). The porphyrin fluorescence of the PLP was effectively silenced (>95% quenching efficiency) due to intermolecular fluorescence quenching caused by high density packing of the porphyrin molecules. Photodynamic activity was also suppressed in the intact PLPs (20). Both fluorescence and photodynamic reactivity can be promptly restored by disruption of the nanostructure. The intrinsic metal chelating capability of the porphyrin allowed for direct labeling with the radionuclide copper-64 through a robust procedure to generate ^{64}Cu-PLPs with a labeling yield greater than 98%.

PLP-PET enabled detection of primary tumor and sentinel lymph nodes in HNC rabbit model

We investigated the feasibility of PLPs for HNC detection and treatment using a VX-2 buccal squamous cell carcinoma rabbit model that is a particularly inimitable model for developing lymphatic metastases within approximately 2 weeks after tumor induction. The blood clearance profile of ^{64}Cu-PLP was fitted to a two-compartment model, showing a favorable slow half-life of 27.7 hours (Fig. 2A). PET imaging was performed on VX-2 rabbits at 24 hours after intravenous injection of ^{64}Cu-PLP (0.34 mg/kg of porphyrin, ~5 mCi) to match its biologic half-life and radionuclide half-life (^{64}Cu $t_{1/2}$ = 12.7 hours). As shown in the PET/CT coregistered image (Fig. 2B, Supplementary Fig. S1), the tumor and sentinel lymph node (SLN) were clearly distinguishable with high contrast. Moreover, the 360° view of the image clearly displays the drainage from tumor to lymph node (Supplementary Video S1), which is unprecedented for intravenous administration of organic nanoparticles. Consistent with the rendered image, tumor and SLN showed significantly higher SUVs quantified from PET volume-of-interest (VOI) measurements compared with that of surrounding muscle, which was 3.58 ± 0.53, 2.57 ± 0.53, and 0.35 ± 0.02, respectively ($n = 5$, $P < 0.05$, Fig. 2C).

The distribution of ^{64}Cu-PLPs in major organs was further evaluated by gamma-counting, which revealed similar distribution patterns in healthy tissues of PLP in tumor-bearing and healthy rabbits (Fig. 2D). The relatively high SUV of the liver (9.34 ± 0.92 SUV and 10.54 ± 1.68 SUV for tumor-bearing and healthy rabbits, respectively) was likely due to hepatobiliary clearance of ^{64}Cu-PLPs. However, this high uptake would not affect HNC detection considering the relatively remote location of the liver from the head and neck region. The average uptake of tumor and SLN from gamma-counting was 3.14 ± 0.26 SUV and 2.21 ± 0.26 SUV, respectively (Fig. 2D, $n = 5$), which is consistent with their corresponding SUVs from PET image VOI quantification (Fig. 2C). The SLN of tumor-bearing rabbits exhibited significantly higher uptake than that of healthy rabbits (0.87 ± 0.13 SUV, $n = 3$, $P < 0.01$) and is likely due to the elevated lymphatic flow and the presence of metastatic lesions that were identified by H&E analysis and PanCK staining (Supplementary Fig. S2). Therefore, ^{64}Cu-PLPs were capable of delineating malignant SLNs from healthy ones.

Ex vivo fluorescence imaging of the resected tissues further confirmed the significantly higher accumulation and fluorescence activation of PLPs in the tumor and draining SLN of tumor-bearing rabbits (Fig. 2E). Negligible fluorescence signal was observed in the salivary glands despite the relatively high accumulation of ^{64}Cu-PLPs (Fig. 2E). This is likely due to PLP nonspecifically accumulating in salivary glands like other PET imaging agents (e.g., ^{18}F-FDG), but remaining intact and nonfluorescent. These results indicate that by utilizing both PET and fluorescence imaging, PLP was able to provide complementary information for accurate detection of metastatic lymph nodes and potentially could be employed for image-guided resection of lymph nodes with low background fluorescence of the salivary glands.

Fluorescence-guided resection of primary tumor and metastatic disease

By taking advantage of the selective fluorescence activation of PLPs in the tumor and metastatic lymph node(s), we evaluated the capacity of PLPs for fluorescence intraoperative guidance of surgical resection of primary tumors and SLN(s) in tumor-bearing rabbits. As shown in Fig. 3A, the tumor (with skin intact) was sufficiently fluorescent for visualization compared with surrounding tissue under an *in vivo* fluorescence imaging system. Upon raising the skin flap during surgical exploration, the tumor was exposed and was clearly delineated by the porphyrin fluorescence (Fig. 3B). Guided by the fluorescence, all suspicious malignancies around the cheek were surgically removed. The surgical bed exhibited negligible fluorescence signal, suggesting complete tumor resection (Fig. 3C). The resected tissues were confirmed to be malignant by histologic analysis (Fig. 3D). The porphyrin fluorescence in the tissue histology slides corresponded well with cancer cell morphology and positive PanCK staining, indicating that PLP fluorescence highlighted the primary tumor with considerable specificity and accuracy at the cellular level (Fig. 3D). Likewise, PLP fluorescence also delineated the draining SLN *in vivo* (Fig. 3E). Notably, the lymphatic network from the primary tumor to SLN, and to regional lymph nodes was exquisitely mapped by the fluorescence signal (Fig. 3F). Following the orientation of the lymphatic network (zoomed-in images, positions 1–5 in Fig. 3F), the secondary positive lymph node and lymphatic spread pattern were identified. Histology-confirmed metastasis in the lymph node and strong porphyrin fluorescence were observed in the PanCK-positive area, indicating uptake of PLP in the metastatic region (Fig. 3G). Altogether, PLP fluorescence not only clearly delineates the primary tumor and malignant lymph node(s), but

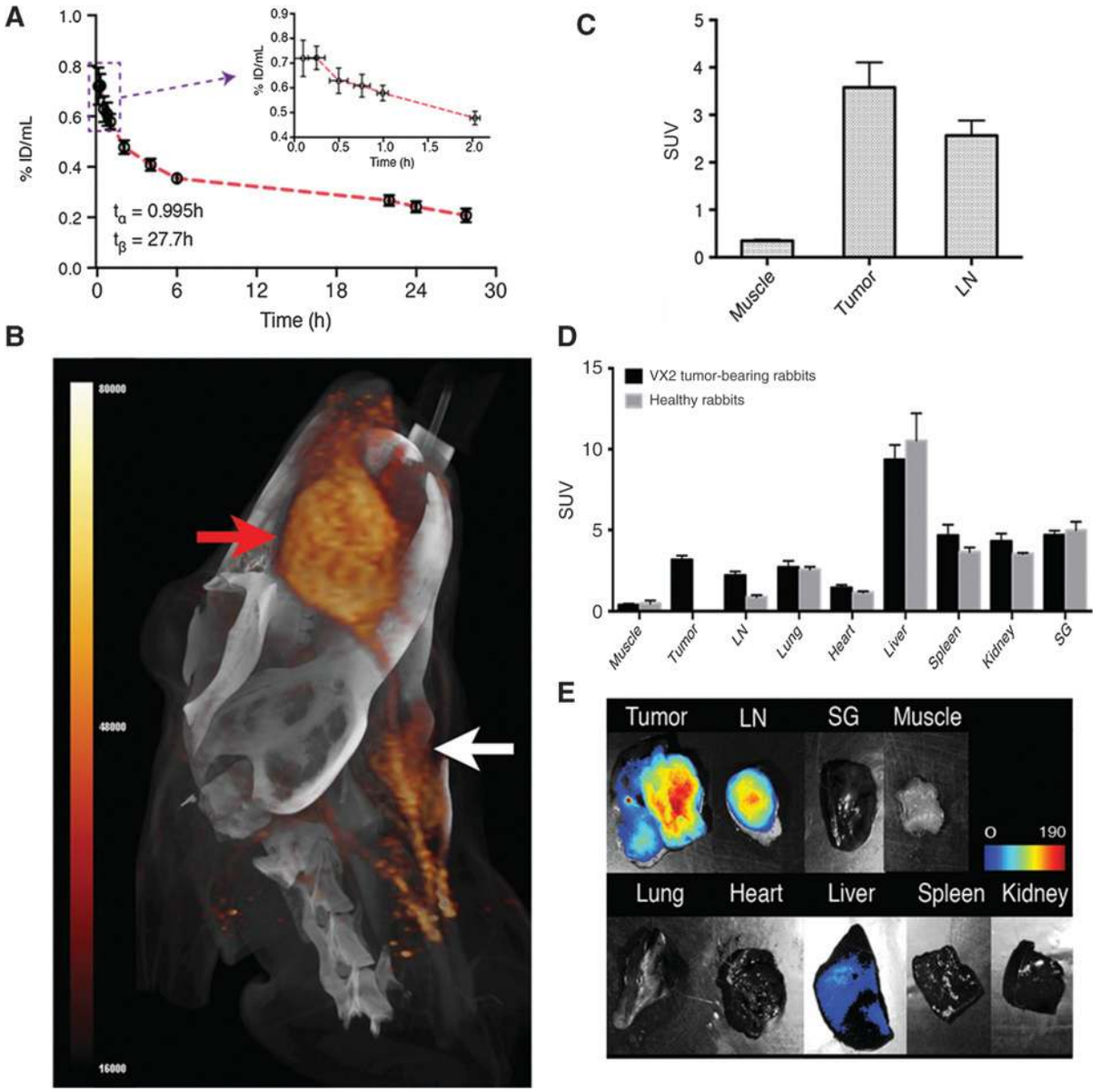

Figure 2.

PLP-enabled noninvasive detection of primary tumor and lymphatic drainage in rabbit HNC model; A, pharmacokinetic profile of PLP in HNC rabbits ($n = 4$); B, representative PET/CT 3D image of HNC rabbit at 24 hours after intravenous injection of ^{64}Cu-PLP (red arrow: tumor, white arrow: regional lymph node); C, distribution of ^{64}Cu-PLP in muscle, tumor and lymph node quantified by PET volumetric analysis. The uptake was presented as SUVs. Tumor and lymph node uptake of PLP were significantly higher than the muscle uptake ($n = 4$, $P < 0.05$); D, distribution of ^{64}Cu-PLP in major organs in HNC rabbits ($n = 5$) and healthy rabbits ($n = 3$) measured by γ-counting; E, *ex vivo* fluorescence of resected tumor, regional lymph node and other major organs of HNC rabbits after PET/CT imaging.

also the regional lymphatic network, which may potentially aid in nodal staging of HNC patients and reveal malignant lymph nodes prior to resection and pathologic analysis.

PLP-enabled PDT induced apoptosis

By knowing that the fluorescence can be promptly restored upon tumor accumulation, we next investigated whether the photodynamic reactivity of PLPs can be activated efficiently for PDT. PDT effectiveness was first evaluated in a KB xenograft mouse model with four groups, including blank control, PLP control, laser control, and PLP-PDT group ($n = 3$). At 24 hours after intravenous injection of PLP, high-contrast porphyrin florescence was observed in tumor regions, indicating selective tumor accumulation and porphyrin fluorescence activation (Fig. 4A). The fluorescent tumors subsequently received localized PDT laser treatment (671 nm, 100 mW/cm^2, 75 J/cm^2) that did not cause significant temperature increase in the tumor or the surrounding area, demonstrating that there were no photothermal effects of the treatment (Fig. 4B). The PDT efficacy was examined by H&E histologic analysis at 24 hours after PDT, which

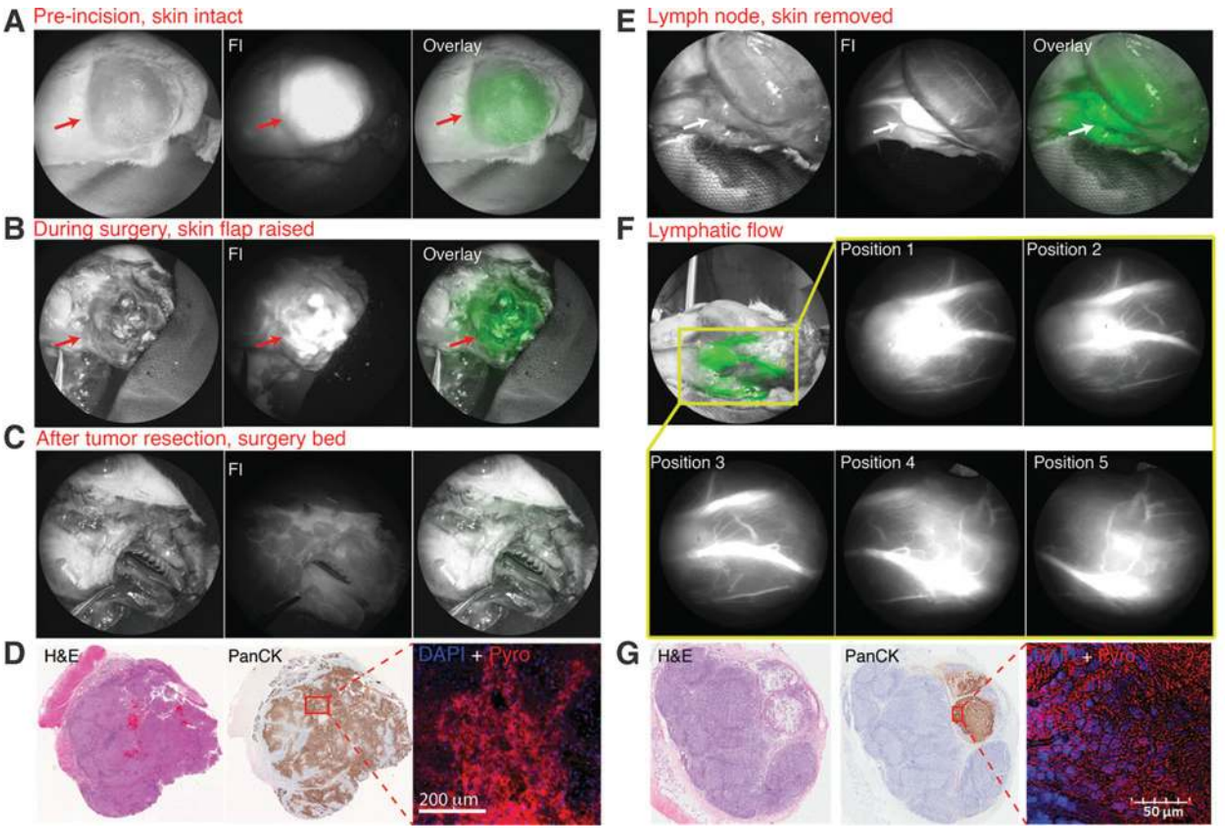

Figure 3.
PLP-enabled fluorescence-guided resection of tumor and metastatic lymph nodes. *In vivo* fluorescence imaging of HNC tumor in rabbits at 24 hours after intravenous injection of PLP: A, before incision with the skin intact; B, during surgery upon skin flap removal; C, postsurgery with the surgical bed nonfluorescent confirming the completion of the procedure; D, representative H&E, Pancytokeratin staining and fluorescence microscopy of tissue slices of the resected tumor; E, intraoperative fluorescence imaging of the sentinel lymph node upon skin flap removal; F, lymphatic network mapped by PLP fluorescence. A series of zoom-in images (position 1–5) were acquired following the lymphatic flow from the sentinel lymph node to the regional lymph node; G, representative H&E, pancytokeratin staining, and fluorescence microscopy of tissue slices of the resected suspicious lymph nodes detected by PLP.

showed that only the PLP-PDT group experienced cellular damage in the tumor, whereas the control groups did not exhibit similar changes (Fig. 4C). The PLP-PDT–induced cell death was further confirmed by a TUNEL assay, which demonstrated that PLP-PDT significantly enhanced cell apoptosis in the tumor (73.2% positive) compared with the control groups (1.5% positive for blank control, 6.9% positive for laser control, and 7.1% positive for PLP control; Fig. 4D). In addition, no obvious cellular damage or morphology changes were observed in the healthy organs of the PLP-PDT–treated groups in comparison with the blank controls (Supplementary Fig. S3), indicating that PLP-enabled PDT does not cause toxicity to healthy tissues.

The long-term therapeutic effect of PLP-PDT was assessed on HNC rabbits. Tumor-bearing rabbits with average tumor sizes of 300 mm^3 were categorized into four groups, including blank control ($n = 3$), laser only control ($n = 3$), PLP only control ($n = 3$), and PLP-PDT group ($n = 4$). As shown in Fig. 5A, a two-step laser irradiation strategy was used for the PDT at 24 hours after PLP injection to irradiate the entire tumor volume. The absence of significant temperature increase during the laser treatment confirmed no thermal effect of the treatment, precluding the concern that thermal effect may cause unintended side effects on neighboring healthy tissues (Supplementary Fig. S4). PLP-PDT caused scarring around the tumor beginning from 24 hours after PDT, until 26 days after treatment. Ultimately, all PLP-PDT rabbits had no palpable tumor at day 34 after treatment (Fig. 5B). Posttreatment tumor volumes were quantitatively determined by the volumetric measurement of three-dimensional microCT images. The PLP-PDT group showed a slight tumor size increase within the first week after treatment, which was likely attributable to the expected inflammatory response and edema caused by PDT (Fig. 5C). However, the tumor size gradually declined from 6 days after PDT until no tumor was detected on day 34 after PDT. In contrast, the control groups that received either laser irradiation or PLP administration alone showed accelerating tumor growth, similar to the blank control, indicating that neither of them induced any therapeutic effects (Fig. 5D and Supplementary Fig. S5). The control groups reached the end point (tumor volume > 5,000 mm^3) at day 6 for blank control, day 8 for laser control, and day 9 for PLP control (Fig. 5D), respectively. PLP-PDT enabled complete tumor ablation was further confirmed by pathologic analysis, which demonstrated that the tissues resected from the original tumor area at terminal surgery did not exhibit pathologic cell morphology, in addition to its negative PanCK staining (Fig. 5E). Notably, although they did not receive direct laser irradiation, the lymph nodes of the PLP-PDT group showed a

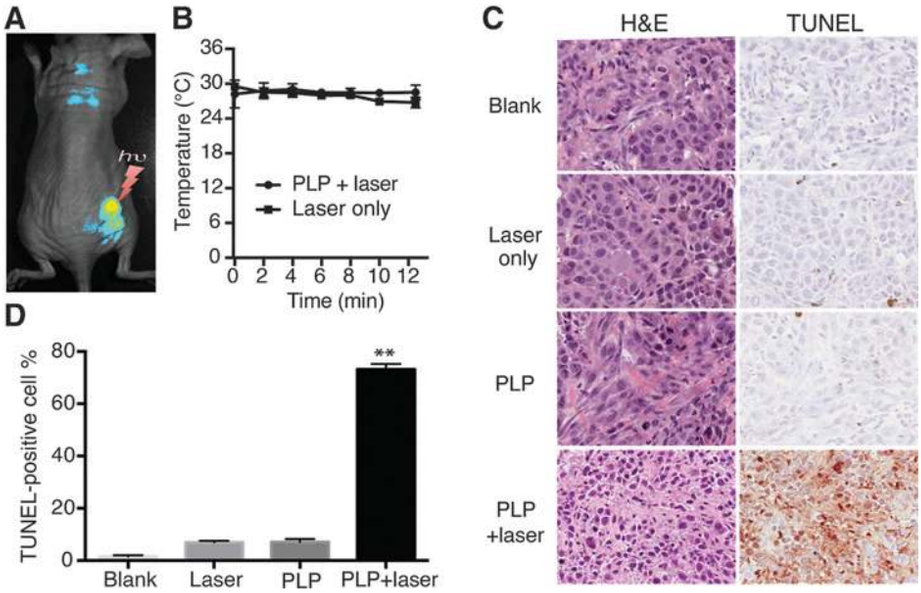

Figure 4.
PLP-enabled PDT in a mouse xenograft model. A, fluorescence activation of PLP in KB xenograft model at 24 hours after intravenous injection of PLP; B, averaged tumor temperature during laser irradiation for laser control and PLP-PDT groups ($n = 3$ for each group); C, H&E and TUNEL staining of tumor sections from blank control, laser control, PLP control, and PLP-PDT groups at 24 hours after treatment; D, percentage of TUNEL-positive cells out of total cells in the tumor region of all groups. Significantly higher cell apoptosis in the tumor was observed in the PLP-PDT group compared with the controls ($n = 3$, $P < 0.05$).

gradual decrease in size from 14 days after PDT (Supplementary Fig. S6). All lymph nodes from the PLP-PDT group were found metastasis-free at 34 days after PDT evidenced by pathology and PanCK staining analysis (Fig. 5F). These results strongly suggest that for HNC subtypes that are surgically inaccessible or adjacent to critical anatomical structures, such as the oropharynx, nasopharynx, hypopharynx and for recurrence cases, PLP-PDT may serve as an alternative approach to radiation treatment and chemotherapy to increase therapeutic efficacy and decrease long-term toxicity. PLP-PDT appears to be exceedingly effective, highly localized, and allows for the preservation of healthy tissue function.

PLP is a safe multifunctional nanoplatform

The toxicity of PLP-PDT to rabbits was assessed by blood tests periodically (Fig. 6A). The hepatic function of rabbits after treatment were normal with no significant changes, except for alkaline phosphatase (ALP), which showed a moderate decrease within the normal range (from 68.1 ± 8.66 to 43.5 ± 9.67 U/L) at 1 week after treatment and returned to the baseline level over time (normal range 12–98 U/L). Red blood cell level remained stable after treatment, indicating that there was no interference with the physiologic regulation of endogenous porphyrin (heme). White blood cell counts also remained unaffected, suggesting that no immunogenic effects were caused by PLP. Post-mortem histologic analysis on PLP-PDT rabbits did not show abnormal cellular morphology in the heart, lung, liver, spleen, adrenal, or muscle (Fig. 6B). These results suggest that PLP-enabled PDT treatment is a safe therapeutic approach.

Discussion

HNC management is often limited by inappropriate tumor detection. In this study, we have shown that PLP nanoparticles could enhance HNC diagnosis and improve therapeutic intervention and management. ^{64}Cu-PLP enabled PET/CT imaging of primary tumors and lymphatic drainage from tumor to metastatic lymph node at 24 hours after intravenous injection in a clinically relevant large animal HNC model. Although some nonspecific uptake of ^{64}Cu-PLP in the salivary gland was detected, selective fluorescence activation of PLP resulted in high fluorescence signals in the tumor and the subsequent lymphatic drainage network, whereas the salivary gland and healthy lymph node(s) displayed background-level fluorescence. Therefore, fluorescence imaging following PET imaging could have tremendous potential to enable tumor localization and determine the invasion status of the draining lymph nodes.

Lymph node metastasis is a significant indicator for low survival and poor prognosis and is predictive of a higher risk for distant metastases (25, 26), which are responsible for most HNC deaths (27). Thus, accurate detection of lymph nodes metastasis close to the primary tumor is fundamental for appropriate treatment, especially for individuals diagnosed with oral cavity or oropharyngeal squamous cell carcinoma (28). However, clinically, it is challenging to evaluate lymph node metastasis status reliably, which results in inappropriate treatment to many of HNC patients (29). For example, elective neck dissection is currently recommended for all HNC patients with an occult metastatic rate greater than 20% to 30%, (30), which actually might not be necessary for 60% to 70% of patients (31, 32) and is associated with high risks and morbidity (33–35). The standard technetium-99–based SLN biopsy procedure currently suffers from several limitations, including lack of real-time intraoperative visual information (36–38). PLPs offer a promising method for accurately detecting malignant SLNs with preoperative PET/CT imaging and complementary fluorescence imaging for noninvasive diagnosis, preoperative stratification, and more accurate cancer staging. In addition, PLP would provide insight of metastatic lymphatic pathways for the identification of unknown primaries and recurrent tumors with greater sensitivity to significantly improve cancer patients' surgical outcome. Furthermore, reliable staging of SLNs with PLP would dramatically decrease unnecessary dissection of the neck.

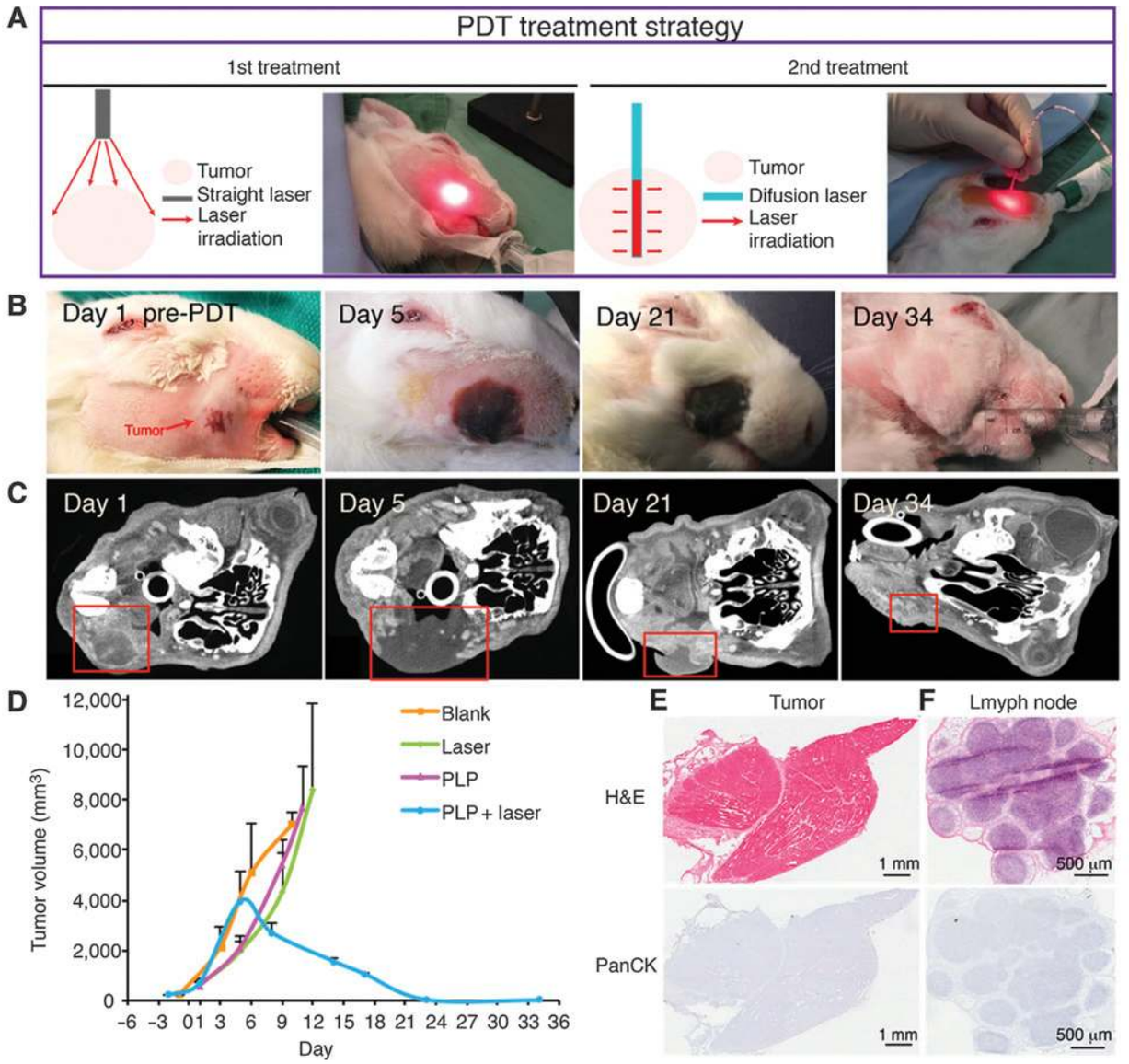

Figure 5.
PLP-enabled PDT in HNC rabbits. A, illustration of the two-step PDT laser irradiation treatment strategy at 24 hours after intravenous injection of PLP; representative photographs (B) and axial CT images (C) of rabbits before and after PLP-PDT; D, average tumor growth curve determined by volumetric CT measurements; representative H&E and Pancytokeratin staining of tissues resected from the original tumor region (E) and lymph node resected (F) at day 34 after PLP-PDT. All tissues showed malignancy free.

HNC surgical management is often limited by inappropriate intraoperative tumor delineation and inability to visualize occult nodal metastasis, which leads to increased tumor recurrence, and decreased survival. PLP-enabled real-time intraoperative fluorescence imaging provides a useful tool for image-guided surgical resection of primary tumor and malignant lymph node(s) to achieve complete disease tissue resections.

PLPs are also capable of enhancing targeted delivery of PDT in tumor-bearing rabbits. PDT may be particularly clinically advantageous for patients with tumors that are surgically inaccessible or adjoining to critical anatomical structures. Moreover, the absence of temperature changes during PDT is excellent for treating tumors close to tissues that are sensitive to heat. Interestingly, all tumor-bearing rabbits at 1 month after PLP-PDT displayed pathologically nonmalignant cervical lymph nodes, though lymph nodes did not receive directly laser irradiation. PLP administration combined with PDT did not result in detectable functional or histologic side effects on rabbits. Therefore, the intrinsic multimodal and biomimetic nature of PLPs confer high potential for clinical translation as a cancer theranostic agent. In addition, the core-shell structure of PLP (hydrophobic core enveloped in hydrophilic shell) provides an amiable environment for stable loading of various cargos, such as chemotherapeutics and siRNAs, thus offering potential for additional chemo- or/and gene therapy. The exact mechanism of PLP uptake into tumors *in vivo* is still not well

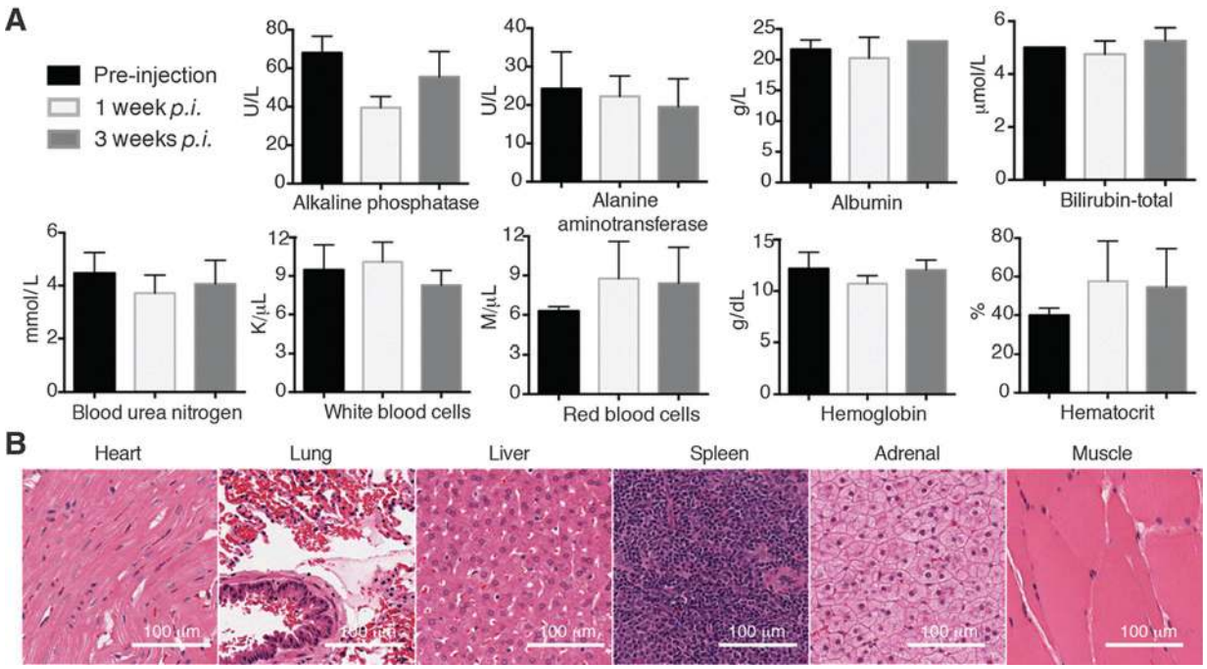

Figure 6.
Evaluation of the toxicity of PLP-PDT. A, blood assay of rabbits before PLP administration and 1 week and 3 week after PLP-PDT treatment ($n = 4$); B, representative H&E staining sections of the main organs, including heart, lung, liver, spleen, adrenal, and muscle from PLP-PDT rabbits, indicating no side effects on healthy tissues after tumor ablation.

understood. One possible explanation for the high tumor selectivity of PLP is a combination of two factors. First, the ultra-small size of PLP (<30 nm) might provide an advantage for efficient penetration through the permeable tumor vasculature into the tumor interstitial space, resulting the local enrichment of porphyrins within the tumor (39). Second, porphyrin molecules have their own tumor affinity that could further drive their selective tumor uptake as reported previously (40).

Conclusion

With the combination of PET imaging, real-time intraoperative NIR fluorescence guidance, and selective PDT intervention, PLPs hold great potential for cancer management. Direct labeling of PLPs with copper-64 enabled accurate, preoperative PET/CT imaging of primary tumors, SLNs, and lymphatic drainage following intravenous administration. The selectively activated fluorescence of PLPs facilitated the accurate delineation of tumors and metastatic lymph nodes. The feasibility of PLPs for intraoperative fluorescence-guided tumor and lymph node resection and tumor-selective PDT were validated in a large HNC animal model. Thus, PLPs provide a multimodal imaging and therapeutic platform that could enhance HNC diagnosis by integrating PET/CT and fluorescence imaging, and improve HNC therapeutic efficacy and specificity by tailoring treatment *via* fluorescence-guided surgical along with selective PDT.

Disclosure of Potential Conflicts of Interest

No potential conflicts of interest were disclosed.

Authors' Contributions

Conception and design: N. Muhanna, L. Cui, H. Chan, F. Wang, J. Chen, J.C. Irish, G. Zheng
Development of methodology: N. Muhanna, L. Cui, C.S. Jin, J. Chen, J.C. Irish
Acquisition of data (provided animals, acquired and managed patients, provided facilities, etc.): N. Muhanna, L. Cui, H. Chan, L. Burgess, T.D. MacDonald, E. Huynh, J. Chen, J.C. Irish
Analysis and interpretation of data (e.g., statistical analysis, biostatistics, computational analysis): N. Muhanna, L. Cui, H. Chan, L. Burgess, C.S. Jin, J. Chen, J.C. Irish, G. Zheng
Writing, review, and/or revision of the manuscript: N. Muhanna, L. Cui, H. Chan, T.D. MacDonald, J. Chen, J.C. Irish, G. Zheng
Administrative, technical, or material support (i.e., reporting or organizing data, constructing databases): N. Muhanna, L. Cui, H. Chan, C.S. Jin, J.C. Irish
Study supervision: N. Muhanna, J. Chen, J.C. Irish, G. Zheng

Acknowledgments

The authors thank the Princess Margaret Cancer Foundation, the Canadian Institutes of Health Research, the Ontario Institute for Cancer Research, the Natural Sciences and Engineering Research Council of Canada, the Canada Foundation for Innovation, Terry Fox New Frontiers Program Project Grant, the major International (Regional) Joint Research Project from National Science foundation of China, and the Joey and Toby Tanenbaum/Brazilian Ball Chair in Prostate Cancer Research for funding this work. In addition, they thank Deborah Scollard and Doug Vines (STTARR Innovation Centre) for imaging and technical support, Sandy Lafrance, Maria Bisa, and the University Health Network animal care staff for their technical services, and Dr. Margarete Akens for donating the VX-2 tumor suspension.

The costs of publication of this article were defrayed in part by the payment of page charges. This article must therefore be hereby marked *advertisement* in accordance with 18 U.S.C. Section 1734 solely to indicate this fact.

Received May 26, 2015; revised September 23, 2015; accepted September 24, 2015; published OnlineFirst October 13, 2015.

References

1. Jemal A, Bray F, Center MM, Ferlay J, Ward E, Forman D. Global cancer statistics. CA Cancer J Clin 2011;61:69–90.
2. Argiris A, Karamouzis MV, Raben D, Ferris RL. Head and neck cancer. Lancet 2008;371:1695–709.
3. Blot WJ, McLaughlin JK, Winn DM, Austin DF, Greenberg RS, Preston-Martin S, et al. Smoking and drinking in relation to oral and pharyngeal cancer. Cancer Res 1988;48:3282–7.
4. Boffetta P, Hecht S, Gray N, Gupta P, Straif K. Smokeless tobacco and cancer. Lancet Oncol 2008;9:667–75.
5. Gandini S, Botteri E, Iodice S, Boniol M, Lowenfels AB, Maisonneuve P, et al. Tobacco smoking and cancer: a meta-analysis. Int J Cancer 2008; 122:155–64.
6. Hashibe M, Boffetta P, Zaridze D, Shangina O, Szeszenia-Dabrowska N, Mates D, et al. Evidence for an important role of alcohol- and aldehyde-metabolizing genes in cancers of the upper aerodigestive tract. Cancer Epidemiol Biomarkers Prev 2006;15:696–703.
7. Miller CS, Johnstone BM. Human papillomavirus as a risk factor for oral squamous cell carcinoma: a meta-analysis, 1982–1997. Oral Surg Oral Med Oral Pathol Oral Radiol Endod 2001;91:622–35.
8. Shiu MN, Chen TH, Chang SH, Hahn LJ. Risk factors for leukoplakia and malignant transformation to oral carcinoma: a leukoplakia cohort in Taiwan. Br J Cancer 2000;82:1871–4.
9. Trubetskoy VS, Cannillo JA, Milshtein A, Wolf GL, Torchilin VP. Controlled delivery of Gd-containing liposomes to lymph nodes: surface modification may enhance MRI contrast properties. Magn Reson Imaging 1995;13:31–7.
10. Valdes Olmos RA, Balm AJ, Hilgers FJ, Koops W, Loftus BM, Tan IB, et al. Thallium-201 SPECT in the diagnosis of head and neck cancer. J Nucl Med 1997;38:873–9.
11. Buck AK, Schirrmeister H, Hetzel M, Von Der Heide M, Halter G, Glatting G, et al. 3-deoxy-3-[(18)F]fluorothymidine-positron emission tomography for noninvasive assessment of proliferation in pulmonary nodules. Cancer Res 2002;62:3331–4.
12. Rajendran JG, Mankoff DA, O'Sullivan F, Peterson LM, Schwartz DL, Conrad EU, et al. Hypoxia and glucose metabolism in malignant tumors: evaluation by [18F]fluoromisonidazole and [18F]fluorodeoxyglucose positron emission tomography imaging. Clin Cancer Res 2004;10:2245–52.
13. Van de Wiele C, Lahorte C, Oyen W, Boerman O, Goethals I, Slegers G, et al. Nuclear medicine imaging to predict response to radiotherapy: a review. Int J Radiat Oncol Biol Phys 2003;55:5–15.
14. Thorek DL, Ulmert D, Diop NF, Lupu ME, Doran MG, Huang R, et al. Non-invasive mapping of deep-tissue lymph nodes in live animals using a multimodal PET/MRI nanoparticle. Nat Commun 2014;5:3097.
15. Dolmans DE, Fukumura D, Jain RK. Photodynamic therapy for cancer. Nat Rev Cancer 2003;3:380–7.
16. Lovell JF, Liu TW, Chen J, Zheng G. Activatable photosensitizers for imaging and therapy. Chem Rev 2010;110:2839–57.
17. Jin CS, Cui L, Wang F, Chen J, Zheng G. Targeting-triggered porphysome nanostructure disruption for activatable photodynamic therapy. Adv Healthc Mater 2014;3:1240–9.
18. Dougherty TJ, Gomer CJ, Henderson BW, Jori G, Kessel D, Korbelik M, et al. Photodynamic therapy. J Natl Cancer Inst 1998;90:889–905.
19. Wilson BC, Patterson MS. The physics, biophysics and technology of photodynamic therapy. Phys Med Biol 2008;53:R61–109.
20. Cui L, Lin Q, Jin CS, Jiang W, Huang H, Ding L, et al. A PEGylation-Free Biomimetic Porphyrin Nanoplatform for Personalized Cancer Theranostics. ACS Nano 2015;9:4484–95.
21. Jin CS, Lovell JF, Chen J, Zheng G. Ablation of hypoxic tumors with dose-equivalent photothermal, but not photodynamic, therapy using a nanostructured porphyrin assembly. ACS Nano 2013;7:2541–50.
22. Lovell JF, Jin CS, Huynh E, Jin H, Kim C, Rubinstein JL, et al. Porphysome nanovesicles generated by porphyrin bilayers for use as multimodal biophotonic contrast agents. Nat Mater 2011;10:324–32.
23. Li SJ, Ren GX, Jin WL, Guo W. Establishment and characterization of a rabbit oral squamous cell carcinoma cell line as a model for in vivo studies. Oral Oncol 2011;47:39–44.
24. Lin LM, Chen YK, Chen CH, Chen YW, Huang AH, Wang WC. VX2-induced rabbit buccal carcinoma: a potential cancer model for human buccal mucosa squamous cell carcinoma. Oral Oncol 2009;45:e196–203.25.
25. Lucey BC, Stuhlfaut JW, Soto JA. Mesenteric lymph nodes seen at imaging: causes and significance. Radiographics 2005;25:351–65.
26. Pagliarulo V, Hawes D, Brands FH, Groshen S, Cai J, Stein JP, et al. Detection of occult lymph node metastases in locally advanced node-negative prostate cancer. J Clin Oncol 2006;24:2735–42.
27. Hasegawa T, Tanakura M, Takeda D, Sakakibara A, Akashi M, Minamikawa T, et al. Risk factors associated with distant metastasis in patients with oral squamous cell carcinoma. Otolaryngol Head Neck Surg 2015;156:1053–63.
28. Pantel K, Brakenhoff RH. Dissecting the metastatic cascade. Nat Rev Cancer 2004;4:448–56.
29. Forastiere A, Koch W, Trotti A, Sidransky D. Head and neck cancer. N Engl J Med 2001;345:1890–900.
30. Nieuwenhuis EJ, Castelijns JA, Pijpers R, van den Brekel MW, Brakenhoff RH, van der Waal I, et al. Wait-and-see policy for the N0 neck in early-stage oral and oropharyngeal squamous cell carcinoma using ultrasonography-guided cytology: is there a role for identification of the sentinel node? Head Neck 2002;24:282–9.
31. Leusink FK, van Es RJ, de Bree R, Baatenburg de Jong RJ, van Hooff SR, Holstege FC, et al. Novel diagnostic modalities for assessment of the clinically node-negative neck in oral squamous-cell carcinoma. Lancet Oncol 2012;13:e554–61.
32. Weiss MH, Harrison LB, Isaacs RS. Use of decision analysis in planning a management strategy for the stage N0 neck. Arch Otolaryngol Head Neck Surg 1994;120:699–702.
33. Bradley PJ, Ferlito A, Silver CE, Takes RP, Woolgar JA, Strojan P, et al. Neck treatment and shoulder morbidity: still a challenge. Head Neck 2011;33:1060–7.
34. van Wilgen CP, Dijkstra PU, van der Laan BF, Plukker JT, Roodenburg JL. Morbidity of the neck after head and neck cancer therapy. Head Neck 2004;26:785–91.
35. van Wouwe M, de Bree R, Kuik DJ, de Goede CJ, Verdonck-de Leeuw IM, Doornaert P, et al. Shoulder morbidity after non-surgical treatment of the neck. Radiother Oncol 2009;90:196–201.
36. Burcia V, Costes V, Faillie JL, Gardiner Q, de Verbizier D, Cartier C, et al. Neck restaging with sentinel node biopsy in T1-T2N0 oral and oropharyngeal cancer: Why and how? Otolaryngol Head Neck Surg 2010;142: 592–7 e1.
37. de Rosa N, Lyman GH, Silbermins D, Valsecchi ME, Pruitt SK, Tyler DM, et al. Sentinel node biopsy for head and neck melanoma: a systematic review. Otolaryngol Head Neck Surg 2011;145:375–82.
38. Koch WM, Choti MA, Civelek AC, Eisele DW, Saunders JR. Gamma probe-directed biopsy of the sentinel node in oral squamous cell carcinoma. Arch Otolaryngol Head Neck Surg 1998;124:455–9.
39. Huynh E, Zheng G. Cancer nanomedicine: addressing the dark side of the enhanced permeability and retention effect. Nanomedicine 2015;10: 1993–5.
40. Chen Y, Gryshuk A, Achilefu S, Ohulchansky T, Potter W, Zhong T, et al. A novel approach to a bifunctional photosensitizer for tumor imaging and phototherapy. Bioconjug Chem 2005;16:1264–74.